Raman Spectroscopy for Spinline Crystallinity Measurements. II. Validation of Fundamental Fiber-Spinning Models

Rajen M. Patel, Antonios K. Doufas,* Rajesh P. Paradkar

Dow Chemical Company, Freeport, TX 77541

Received 6 December 2007; accepted 18 March 2008
DOI 10.1002/app.28387
Published online 27 May 2008 in Wiley InterScience (www.interscience.wiley.com).

ABSTRACT: The original Doufas–McHugh two-phase microstructural/constitutive model for stress-induced crystallization is expanded to polyolefin systems and validated for its predictive capability of online Raman crystallinity and spinline tension data for two Dow homopolymer polypropylene resins. The material parameters—inputs to the model—are obtained from laboratory-scale material characterization data, that is, oscillatory dynamic shear, rheotens (melt extensional rheology), and differential scanning calorimetry data. The same set of two stress-induced crystallization material/molecular parameters are capable of predicting the crystallinity profiles along the spinline and fiber tension very well overall for a variety of industrial fabrication conditions. The model is capable of predicting the freeze point, which is shown, for the first time, to correlate very well with the measured stick point (i.e., the point in the spinline at which the fiber bundle converts from a solid-like state to a liquid-like state and sticks to a solid object such as a glass rod). The model quantitatively captures the effects of the take-up speed, throughput, and melt flow rate on the crystallization rate of polypropylene due to stress-induced crystallization effects. This validated modeling approach has been used to guide fiber spinning for rapid product development. The original Doufas–McHugh stress-induced crystallization model is shown to be numerically robust for the simulation of steady polypropylene melt spinning over a wide range of processing conditions without issues of discontinuities due to the onset of the two-phase constitutive formulation downstream of the die face, at which crystallization more realistically begins. Because of the capturing of the physics of polypropylene fiber spinning and the very good model predictive power, the approximations of the original Doufas–McHugh model are asserted to be reasonable. © 2008 Wiley Periodicals, Inc. J Appl Polym Sci 109: 3398–3412, 2008

Key words: fibers; modeling; poly(propylene) (PP); Raman spectroscopy

INTRODUCTION

The objective of this article is to present validation of fundamental fiber-spinning models in terms of the predictive capability of online crystallinity data and spinline tension of polyolefin systems. Specifically, two Dow homopolymer polypropylene (hPP) resins are studied in this work, H502-25RG and 5D49. The development of the experimental procedure and its application for measuring fiber crystallinity along the spinline via Raman spectroscopy is documented elsewhere.[1,2] To our knowledge, this is the first work that reports on the online measurement of the spinline absolute crystallinity for hPP fibers. Prior work has focused on the measurement of flow birefringence along the spinline.[3,4] However, birefringence is a convolution of amorphous and crystalline orientation along with crystallinity, and so a direct determination of the spinline crystallinity from birefringence data is very difficult.

The original Doufas–McHugh (D–M) two-phase constitutive/microstructural model for stress-induced crystallization (SIC)[5–7] is used to predict spinline experimental data. A first version of the model and its application to both shear and extensional kinematics are documented elsewhere.[8] A model application to polyamide and poly(ethylene terephthalate) (PET) fiber spinning in both one- and two-dimensional computational domains is described.[5–7] In this article, the D–M model[5–7] is expanded to polyolefin systems and specifically polypropylene (PP), which in general have a different melt rheology (e.g., longer relaxation times) than polyamides and PET and can therefore be numerically more challenging to simulate because of the high Weissenberg numbers (caused by the long relaxation times).[5]

Important aspects of the physics of fiber spinning include the nonlinear melt viscoelasticity under both nonhomogeneous and nonisothermal flow conditions coupled with the SIC kinetics and rheology of the semicrystalline phase; all these elements are included in our constitutive formulation. The model has a

Correspondence to: R. M. Patel (rmpatel@dow.com).
**Present address:* Sunoco, Inc., Pittsburgh, PA 15219.

TABLE I
List of Polymer Resins with the Material Properties

Resin	Molecular structure	MFR (g/10 min)[a]	M_w (g/mol)	M_n (g/mol)	M_w/M_n	Solid density (g/cc)[b]
H502-25RG	hPP, linear	25	173,800	63,600	2.73	0.9
5D49	hPP, linear	38	137,400	42,700	3.22	0.9

[a] ASTM D 1238 (230°C/2.16 kg).
[b] ASTM D 792

molecular basis because it is based on polymer kinetic[9] and nucleation theories and is also consistent with the laws of irreversible thermodynamics.[8] To our knowledge, this model was the first fundamental one to predict the necking phenomenon under high-speed spinning conditions. Its excellent predictive capability for fiber velocity, diameter, temperature, and birefringence profiles under both low- and high-speed spinning conditions has been extensively demonstrated.[5–7] A modified version of the model has been successfully applied and validated in the context of the blown film process[10] and has been also applied to the simulation of injection molding by researchers at Moldflow Pty., Ltd.[11,12] The melt rheology constitutive model was expanded and applied to polyolefin systems in the context of rheotens experiments by Doufas.[13] The last is one building block of the fiber-spinning model presented in this work.

EXPERIMENTAL

Materials

The polymer systems studied in this work along with key material properties are summarized in Table I. The melt flow rate (MFR) was determined according to ASTM D 1238 (230°C, 2.16 kg). The solid density was measured according to ASTM D 792. The molecular mass distribution data were obtained with a Waters (Milford, MA) 150C instrument via both conventional and triple-detector gel permeation chromatography (GPC). Typical GPC data are also listed in Table I. The number-average molecular weight (M_n) data are accurate within 8%, the weight-average molecular weight (M_w) data are accurate within 4%, and the z-average molecular weight data are accurate within 10%.

Dynamic mechanical spectroscopy (DMS) oscillatory shear experiments

DMS oscillatory shear data were generated with a Rheometrics (Piscataway, NJ) RMS-800 system using 25-mm parallel plates in a nitrogen purge. A frequency range of 0.1–100 rad/s at five points per decade was used at temperatures of 190, 210, and 230°C. Strain amplitudes of 10–25% were used for all experiments and lay within the linear viscoelastic regime.

Rheotens experiments

The rheotens data were generated with the ALR 72.2 rheotens setup of Göettfert (Rock Hill, SC).[13] The rheotens device was coupled to an extruder as the melt feeder and a gear pump to stabilize and control the flow rate (up to 10 g/min could be achieved). This had advantages over a piston–capillary melt feeder, in the sense that the extruder could produce higher mass throughputs, which reduced the fiber cooling below the die. The output was verified before the experiments for each resin by the weighing of the extrudate within a certain time period (typically 1 min). A die with a 40/2 length/diameter ratio (dimensions in millimeters) with an entrance angle of 60° was used. Calibration of the rheotens device was performed by the measurement of the tension of weight standards before the experiments and was verified also upon completion of the experiments. A strand was taken up by two wheels rotating at a continuously increasing speed. The acceleration of the speed was 24 mm/s^2. The force needed to elongate the filament was continuously measured by means of a force–displacement system. The reproducibility of the data was very good.[13] The processing conditions of the rheotens experiments are summarized in Table II.

Fiber-spinning experiments[2]

Both resins studied in this work (Table I) were melt-spun at a die temperature of 224 ± 1°C on a pilot-scale Hills line with a 1-in.-diameter bicomponent single-screw extruder with an aspect ratio (length/diameter) of 30:1. Only one side (side A) of the bicomponent extruder was used to spin the fibers, whereas side B was left empty. Constant throughput was maintained with a Zenith (Sanford, NC) 2.87 cc/rev gear pump. The melt pump was operated at 8.3 and 16.6 rpm, yielding throughputs of 0.308 and 0.625 g/min/hole (ghm), respectively. The actual throughput was measured by the setting of the desired pump speed and weighing of the extruded polymer collected for 2 min. A round 60-hole spinneret was used to extrude the fibers. The spinneret

TABLE II
Processing Conditions of the Rheotens Experiments

Processing condition	Value
Die diameter	2 mm
Pull-off velocity	50–1000 mm/s
Wheel acceleration	24 mm/s^2
Mass throughput	10 g/min
Die temperature	190°C
Spinline length	10 cm
Length between take-up wheels and floor	85 cm
Surrounding air temperature	20°C
Quench air velocity (cross or downward)	0 m/s

capillary length and diameter were 0.381 and 2.29 mm, respectively. The fibers were quenched with cooling air blown perpendicularly to the direction of filament flow. The quench zone was 183 cm long and was located 12.7 cm below the spinneret (quench delay). The temperature of the quenching air, measured with a hot-wire anemometer, was 15.4 ± 1°C, and the average air velocity across the quench zone was 0.17 m/s. The fibers were passed around a take-up roll, located 419 cm below the spinneret, and finally taken up on a bobbin with a Barmag SW4 winder.

Stick-point measurements

Stick point is defined as the point in the spinline at which the fibers transition from a solid-like state to a liquid-like state, which results in fibers sticking to a solid object. We measured the stick points by stringing up the fibers at a fixed take-up speed and then pressing a glass rod against the front of the fiber bundle at the bottom of the quench cabinet. The glass rod was gradually raised until the fibers stuck to the rod. The stick point was taken as the distance down from the spinneret face to the point at which the fibers stuck on the glass rod. Special care was taken to move the glass rod across the fiber bundle at a consistent speed. With this procedure, the measured stick points were reproducible within ~±5–10 cm.

Fiber tension measurements

Fiber tension was measured near the take-up roll online with a Checkline model DTMX-200 digital tensiometer (Cedarhurst, NY) (0.1–200 gf). The tensiometer was properly calibrated according to National Institute of Standards and Technology standards. The calibration was confirmed by the measurement of the force of a 20-g standard weight. Because of fiber movement and vibrations, the variability of the tension data was estimated to be of the order of 20% (see also the Results and Discussion section).

Raman crystallinity measurements[2]

Raman spectra were acquired on a Kaiser Optical Systems (Ann Arbor, MI) holoprobe Raman spectrometer equipped with a remote fiber optic probe. The Raman probe was mounted on an xyz translation stage that was in turn mounted on a tripod. Different locations along the spinline were accessed by the raising or lowering of the tripod and/or the z translation. Because the side-to-side movement of the fibers in the quench tower significantly reduced the Raman signal, a low-friction ceramic guide was used to stabilize the fibers during the Raman measurements. Raman spectra were acquired from the fiber bundle.[2] All the spectral acquisition was performed with Holograms, and the spectra were subsequently transferred to Grams/AI for processing and analysis. Additional details on the online crystallinity measurements using Raman spectroscopy are presented in a companion publication.[2]

Differential scanning calorimetry (DSC) experiments

Thermal measurements were performed on a TA Instruments (New Castle, DE) Q1000 differential scanning calorimeter. Measurements were made on both pellet samples for the determination of quiescent crystallization kinetics needed for model simulations and fiber calibration samples for the measurement of crystallinity and comparison with Raman spectroscopy measurements. The instrument was calibrated with indium (melting point = 156.6°C, heat of fusion = 28.4 J/g) following standard procedures. For the measurement of the crystallization rate from pellets, specimens weighing 5–10 mg were first heated at 230°C in DSC aluminum pans, in which the samples were equilibrated for 3 min. This is well above the equilibrium melting point (T_m^0) for PP (≈187°C)[14] and serves to erase the prior thermal history, provide a common starting point, and, very importantly, destroy all traces of crystallinity from residual tiny ordered regions. The crystallization rate was measured through the cooling of the sample from 225 to −40°C at a rate of 10°C/min. The specimen was then heated from −40 to 225°C at 10°C/min to examine the subsequent melting behavior. For such small samples, thermal lag effects are considered negligible.[15] For the fiber samples, typically 3–7 mg of the sample was heated at 10°C/min. The heat of fusion from the first heat was used to calculate the fiber crystallinity. A value of 165 J/g was used for the heat of fusion corresponding to a perfect PP crystal.[14]

MATH MODELING

The original D–M[5–7] constitutive model formulation for fiber spinning was employed to simulate the hPP

experiments studied in this work. The philosophy of the model is the coupling of the filament transport equations (mass, momentum, and energy) using the thin filament approximation with a two-phase constitutive/microstructural formulation for SIC based on polymer kinetic[9] and nucleation theories. Because the mathematical formulation has been extensively documented elsewhere,[5–7] the model equations are not repeated here.

For numerical effectiveness, the inverse Langevin function (L^{-1}), taking into account finite chain extensibility, is calculated with a Pade analytical approximation developed by Cohen at Dow.[16] For example, in the melt phase before crystallization, the nonlinear chain force factor (E) is calculated as follows:

$$E = \frac{L^{-1}(e)}{3e} \approx \frac{1}{3}\frac{3 - e^2}{1 - e^2}, e = \frac{(tr\mathbf{c})^{1/2}}{N_o l} \quad (1)$$

where e represents the fractional chain extension, with the numerator being the average chain end-to-end distance and the denominator being the chain contour length and thus maximum chain extension; N_o is the number of statistical segments per network chain; l is the length of each statistical segment; $tr\mathbf{c}$ is the trace of the $\mathbf{c}$; and $\mathbf{c}$ is the conformational tensor of the amorphous phase representing the second moment of the end-to-end distance of the polymer chains. E is consistently corrected after the onset of the crystallization to account for the loss of melt amorphous statistical segments (rendering the amorphous phase more resistant to stretching) by the coupling of E to the degree of phase transformation (x) and by the proper definition of $\mathbf{c}$ with respect to the remaining melt amorphous segments [$N_o(1 - x)$] at each point of the computational domain.[5,8] The boundary conditions and numerical methods have been described by Doufas et al.[5]

Convective heat-transfer and air-drag coefficients are critical for the simulation of fiber spinning to be successful in achieving quantitative agreement with spinline data, such as fiber velocity, temperature, and crystallinity profile data. Traditionally, empirical heat-transfer relations are employed that are based on the correlation originally developed by Matsui.[17,18] The air-drag coefficient is then determined from the heat-transfer coefficient according to the momentum–heat analog.[19] The available heat-transfer correlations are primarily applicable to monofilament fiber-spinning processes.[19] Anecdotal evidence suggests that heat-transfer rates given by the Matsui correlation may be too high, but (probably for proprietary reasons) there has been little published discussion on this issue.[19]

The challenge in this work is how to calculate the Nusselt number (Nu) and air-drag coefficients for the case of multifilament fiber spinning (60 filaments in our study). Modeling efforts for multifilament melt spinning have been rather limited in the literature. In a multifilament system, complex interactions between the filament bundle and the quench air flow may occur, resulting in variations of the cooling profile from fiber to fiber in the bundle and therefore spun fiber properties. Dutta[20] developed a model for multifilament melt spinning of PET fibers based on the approach of Yasuda et al.[21] In the multifilament model, empirical heat-transfer and air-drag coefficient correlations applied to the monofilament case were employed; however, the quench air velocity was reduced from fiber row to row as the air transversed the filament bundle, whereas the quench air temperature was assumed to be constant within the bundle. The quench air velocity was adjusted for each filament row by the application of local mass balances for the quench air phase. Along similar lines, Ishihara et al.[22] developed a model for a multifilament air-jet melt-spinning process by estimating the profiles of the quench air velocity and temperature from filament to filament in the bundle via the air phase mass and energy balances and applying those profiles to the standard heat-transfer and air-drag correlations corresponding to the monofilament case. Harvey and Doufas[23] developed a computational fluid dynamics approach coupled with a fiber-spinning model to estimate convective heat-transfer coefficients in a multifilament system of up to 1000 filaments. In this study, we apply a lumped approach, in which a corrected average Nu value is used for all 60 filaments studied as follows:

$$Nu_{\text{multifilament}} = \frac{h_{\text{multifilament}} D}{\alpha_a} \approx \kappa_l \, Nu_{\text{monofilament}} \quad (2)$$

where $Nu_{\text{multifilament}}$ is the Nusselt number of the multifilament system, $h_{\text{multifilament}}$ is the average convective heat-transfer coefficient between the 60 filaments, D is the fiber diameter at position z, α_a is the air thermal conductivity, and κ_l is a correction geometrical factor that takes into account the interactions between the multiple filaments with the quench air, and $Nu_{\text{monofilament}}$ is the Nusselt number of the monofilament system. In this work, κ_l is treated as an adjustable process parameter. It is calibrated so that the model matches the spinline tension at the take-up wheel under one set of process conditions (0.625 ghm and 750 m/min for the 5D49 resin). A value of $\kappa_l \approx 0.31$ was determined with this procedure and used in all simulations. Subsequently, the same value of κ_l was used to predict the tension and crystallinity profiles for all other process conditions and resins. A value of $\kappa_l < 1$ makes physical sense, as multiple filaments are expected to cool more slowly than a monofilament spun under the same process conditions.

TABLE III
Melt Rheology/Material Parameters: Inputs for Model Simulations for the hPP Melts

	Laboratory rheological experiment	H502-25RG	5D49
η_0 (Pa s)	DMS	1400	710
E_{act} (kcal/mol)	DMS	9.2	9.2
T_{ref} (°C)	DMS	190	190
G (Pa)	Rheotens	2000	2000
α	Rheotens	0.3	0.3
N_o	Rheotens	25	25

In agreement with the lumped approach for the heat-transfer and air-drag correlations, we considered an average tensile force for each of the 60 filaments. With this approximation, the total spinline tension (F_t) was estimated at the position of the take-up wheels as follows:

$$F_t \approx 60A(\tau_{zz} - \tau_{rr}) \tag{3}$$

where $\tau_{zz} - \tau_{rr}$ is the extra tensile stress difference per filament including contributions from both the amorphous and semicrystalline phases and A is the cross section of the fiber at the end of the spinline.[5,6]

INPUT PARAMETERS

There are of two types of input parameters in the model: (1) material/molecular parameters (including rheological parameters, quiescent crystallization parameters, SIC parameters, and polymer physical properties) and (2) fabrication/process parameters. They are summarized in Tables III–VII.

Melt rheology parameters

There are five material/rheological parameters that describe the melt rheology:[5,13] the zero-shear-rate viscosity at a reference temperature [$\eta_0(T_{ref})$]; the activation energy for flow (E_{act}); the characteristic modulus of elasticity (G), which is considered independent of temperature (the entire temperature dependence is incorporated into the characteristic relaxation time); the molecular mobility parameter (α); and the chain extensibility parameter (N_o).

TABLE IV
Quiescent (Thermal) Crystallization Parameters for hPP

Quiescent crystallization parameter	H502-25RG	5D49
n[a]	3	3
K_{max} (s^{-1})	0.2	0.2
T_{max} (°C)	72	72
D (°C)	50	50

[a] The value under quiescent conditions is listed. Under flow conditions, it is taken to be 1, unless otherwise indicated.

TABLE V
SIC Material Parameters for the Resins Studied

SIC parameter	H502-25RG	5D49
ξ	0.026	0.026
F	300	300

The zero-shear-rate viscosity (η_0) of the polymer melt is calculated according to the Arrhenius relationship and the time–temperature superposition principle as follows:[24]

$$\eta_0(T) = \eta_0(T_{ref}) \exp\left[\frac{E_{act}}{R}\left(\frac{1}{T} - \frac{1}{T_{ref}}\right)\right] \tag{4}$$

where R is the ideal gas constant. The parameters η_0 and E_{act} were obtained from isothermal DMS frequency sweep shear data at various temperatures (at least three are required). The parameter η_0 was determined from the discrete relaxation spectrum as follows:[24]

$$\eta_0 = \sum_{j=1}^{M} \lambda_j G_j \tag{5}$$

where λ_j is a discrete relaxation time of the spectrum, G_j is the corresponding shear modulus, and M is the number of modes. The discrete relaxation spectrum (λ_j, G_j) was obtained with a linear least-square technique from the storage and loss moduli as a function of the angular frequency as outlined elsewhere.[24] E_{act}, determined from the DMS data (9.2 kcal/mol), is quantitatively consistent with a typical value reported by Bird et al.[24] for PP (10.2 kcal/mol).

Nonlinear melt viscoelastic parameters

The material rheological parameters G, α, and N_o, related to the molecular characteristics of the melt, are determined by the fitting of the steady-state portion (before the onset of draw resonance) of a single rheotens force curve (corrected for gravity of the falling filament) for H502-25RG hPP as described in a

TABLE VI
Polymer Physical Properties: Inputs to the Model for 5D49 and H502-25RG hPP Resins

Polymer physical property	5D49 and H502-25RG
ρ (melt) (k/m^3)	760
C_{l1} (cal/g °C)[31]	0.484
C_{l2} (cal/g $°C^2$)[31]	0.00065
C_{s1} (cal/g °C)[31]	0.352
C_{s2} (cal/g $°C^2$)[31]	0.00114
T_m^0 (°C)[14]	187
ΔH_f (J/g)[14]	165
ϕ_∞ [eq. (10)]	55%
Thermal conductivity (W/m K)[31]	0.146
Surface tension (N/m)[31]	0.0219

TABLE VII
Processing Conditions Needed for the Model Simulations

Processing condition	Value
Die diameter	0.38 mm
Number of holes in the spin pack	60
Take-up velocity (m/min)	750, 1000, 1500 m/min
Mass throughput	0.31 and 0.625 ghm
Temperature at the die exit	190°C
Quench delay length	5 cm
Active quench chamber length	106 cm
Spinline length	419 cm
Cross velocity of quench air	0.17 m/s
Downward velocity of quench air	0
Quench air temperature	15.4°C

recent article by Doufas.[13] The corrected force due to the weight of the hanging filament below the wheels was estimated according to the formula of Doufas[13] and found to be in the range of 0.1–0.8 cN (higher at lower take-up speeds and lower at higher speeds). These results are in line with the work of Ghijsels and Chippeleir,[25] who also corrected the rheotens data of various hPPs for the weight of the extrudate hanging between the take-up wheels and the conveying belt, with the magnitude of the correction force varying in the range of 0.2–0.6 cN. Best fit sets were determined by trial and error as described by Doufas[13] and are shown in Table III. Because both H502-25RG and 5D49 resins belong to the same polymer family (hPP) and both have a linear molecular structure (no chain branching), we postulate that both can be rheologically represented by the same set of G, α, and N_o parameters. The only difference between the two resins is η_0, reflecting the difference in MFR. The tensile force versus pull-off speed for H502-25RG is shown in Figure 1. The tensile force increases with the pull-off speed and reaches more or less a plateau (melt strength) at a critical wheel speed. The model fit of the rheotens data is very good, as shown in Figure 1. An apparent elongational viscosity flow curve was estimated with the rheotens model of Doufas[13] and is shown in Figure 2. As depicted in Figure 2, the elongational viscosity presents a relatively prolonged plateau almost corresponding to the Trouton viscosity (no strain hardening) for strain rates up to ~20 s^{-1}, above which the melt shows a mild extensional thinning behavior. This extensional rheology behavior is typical of that of a linear structure melt.[13,26,27] Finally, similar rheological behavior has been observed by Muke et al.[28] for PP melts of MFR similar to those studied in this work.

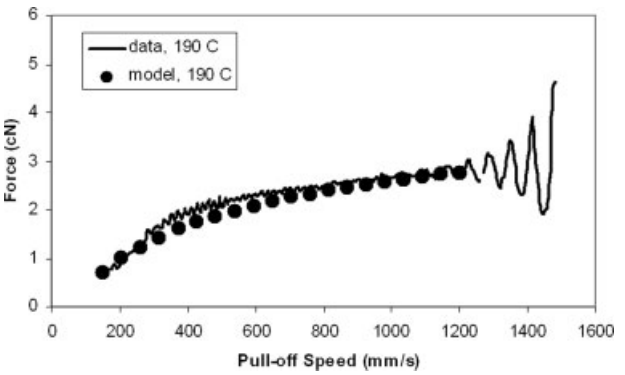

Figure 1 Tensile force versus the pull-off speed (data) and fit of the Doufas rheotens model[13] for the H502-25RG hPP resin. 190°C refers to the die temperature.

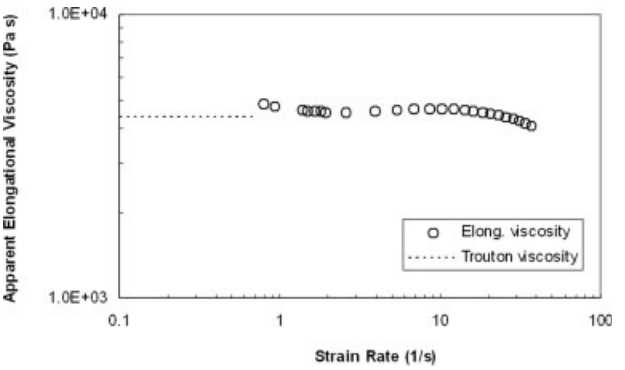

Figure 2 Estimated apparent elongational viscosity versus the strain rate for H502-25RG from the rheotens data of Figure 1 by use of the Doufas rheotens model.[13] The elongational and Trouton viscosities were calculated at the positions of the take-up wheels.

Quiescent crystallization parameters

Consistent with the approach proposed by Patel and Spruiell,[29] the Nakamura model was used here in combination with constant-ramp-rate (nonisothermal) DSC experiments to obtain the quiescent (thermal) crystallization parameters of the model. Nakamura et al.[30] extended Avrami's original isothermal crystallization model to nonisothermal conditions by proposing the isokinetic condition, by which the time dependence of the linear crystal growth rates is equal to the time dependence of nucleation rates. The differential form of the Nakamura equation is described by the following equation:

$$\frac{dx}{dt} = n\,K_{av}(T)[-\ln(1-x)]^{(n-1)/n}(1-x) \qquad (6)$$

where t is the time and x is the degree of phase transformation (relative crystallinity), K_{av} is a crystallization rate parameter (temperature-dependent), and n is the Avrami exponent related to the geometry of crystal growth.[31]

At a constant cooling rate of $dT/dt = q$, which is typical of a nonisothermal (annealed) DSC experiment, and with the application of the chain rule of differentiation to eq. (6), an nonisothermal Avrami-like equation, like that proposed by Nakamura et al.,[30] is given by

$$\frac{dx}{dT} = \frac{1}{q} n\, K_{av}(T)[-\ln(1-x)]^{(n-1)/n}(1-x) \qquad (7)$$

The thermal crystallization rate parameter $K_{av}(T)$ is calculated according to the following equation:[32]

$$K_{av}(T) = K_{\max} \exp\left[-4 \ln 2 \frac{(T - T_{\max})^2}{D^2}\right] \qquad (8)$$

where $K_{\max}$ is a kinetic constant parameter corresponding to the maximum growth rate, $T_{\max}$ is the temperature at which $K_{av} \equiv K_{\max}$, and D is the half-width of the $K_{av}(T)$ curve.[32]

x is calculated from the enthalpies (heat flow) by the integration of the area between the DSC exotherm (cool) and a linear baseline extrapolated from the melt state to the upper limit of the transition as follows:

$$x(T) = \frac{\int_{T_m^o}^{T} H(T')dT'}{\int_{T_m^o}^{T_f} H(T')dT'} \qquad (9)$$

where T_f is the temperature corresponding to the intercept of the exotherm with the baseline in the region of the glass-transition temperature. The integrations were performed with a generalized trapezoidal rule.

The absolute degree of crystallinity (ϕ_∞; maximum achievable) is calculated from the DSC data according to the following equation:

$$\phi_\infty = \frac{\int_{T_m^o}^{T_f} H(T')dT'}{H_f} \qquad (10)$$

where $H(T')$ is the enthalpy at an arbitrary temperature T', and H_f is the heat of fusion of the 100% crystalline polymer (165 J/g for hPP[14]). An approximate value of 55% was estimated for ϕ_∞ for both H502-25RG and 5D49 resins.

By the combination of eqs. (7)–(9), there are four crystallization parameters to be determined from the fitting of the integrated DSC cooling curve [$x(T)$], namely, Avrami exponent n under quiescent conditions, $T_{\max}$, $K_{\max}$, and D. The parameters were determined via a particle swarm optimization procedure.[33] n under quiescent condition is 3, which is consistent with a spherulitic crystal structure. Under flow conditions and because of the uniaxial molecular orientation, n is taken to be 1.[6] The effect of n on the predicted spinline crystallinity profiles is discussed in the Results and Discussion section. An example of the raw DSC exotherm and the best fit $x(T)$ curve for 5D49 hPP is demonstrated in Figure 3. Thermal quiescent crystallization is shown to be primary overall, whereas secondary crystallization effects are shown to be negligible (Fig. 3), as expected for hPP. Best fit quiescent crystallization parameters are shown in Table IV.

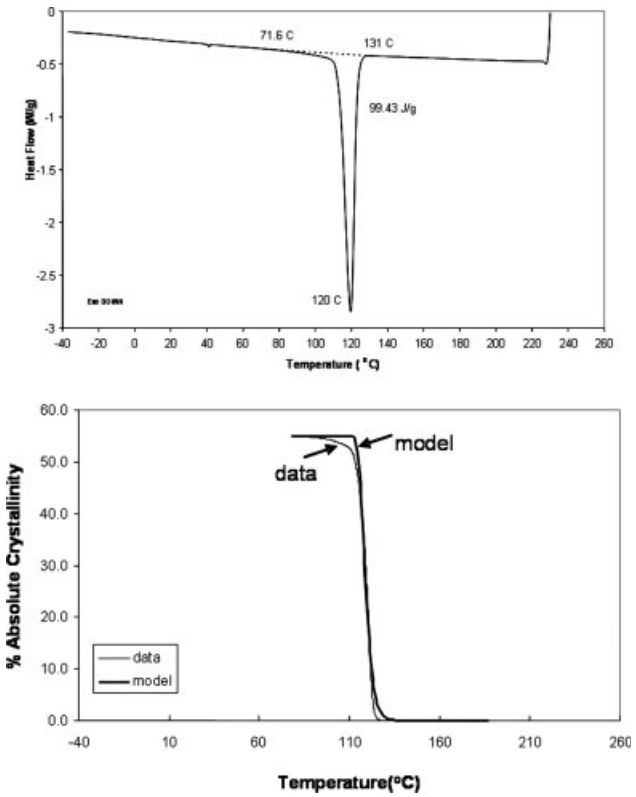

Figure 3 DSC thermograph showing the crystallization exotherm of the 5D49 resin (top) and the fit of the quiescent crystallization parameters from the crystallinity profile (bottom).

SIC parameters

There are two material/molecular parameters related to SIC:[5–7] ξ controls the enhancement of the rate of crystallization by orientational stress and F controls the increase in the relaxation time of the semicrystalline phase during the course of solidification. In this work, ξ and F were determined by trial and error by the fitting of one set of process conditions (750 m/min, 0.625 ghm) for 5D49. Subsequently, the same set of parameters was used for the prediction of other processing conditions and the resin H502-25RG. The values of ξ and F are summarized in Table V. The fact that the crystallinity profiles in the spinline can be predicted with the same set of ξ and F parameters for both H502-25RG and 5D49 resins is

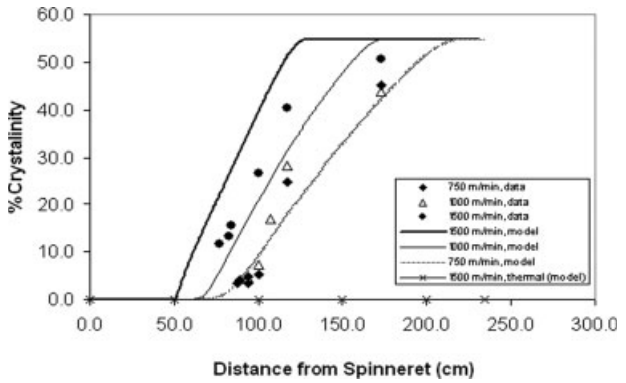

Figure 4 Measured and predicted crystallinity profiles along the spinline as a function of the take-up speed at 0.625 ghm for 5D49.

consistent with the similar molecular microstructures of the two resins and emphasizes the self-consistency of our model and its predictive power.

Rheological parameters for the semicrystalline phase

There are two parameters related to the rheology of the semicrystalline phase: parameter c appearing in the expression for the semicrystalline orientational relaxation time and anisotropic drag parameter σ.[5] Model predictions were found to be practically insensitive to both of these parameters. For c, a value of 0.005 is used as suggested previously.[6] The material parameter σ mostly affects the molecular orientation of the semicrystalline phase but was found not to affect the tensile stress controlling the SIC rate in the model. Therefore, for consistency, a value of $\sigma = 0.5$ was used for all simulations and resins studied in this work.

Polymer physical properties

The heat capacity (C_p) is expressed as a function of the crystallinity and temperature as follows:

$$C_p = C_s x\phi_\infty + C_l(1 - x\phi_\infty) \quad (11)$$

where C_s is the heat capacity of the crystalline regions and C_l is the heat capacity of the amorphous regions. C_s and C_l are represented, in general, as linear functions of the temperature [T (°C)]:

$$C_s(T) = C_{s1} + C_{s2}T \quad (12)$$

$$C_l(T) = C_{l1} + C_{l2}T \quad (13)$$

For the melt density (ρ), an average value of 760 kg/m^3 was used;[13] however it was found that this parameter did not have a significant effect on the model predictions. The parameters of eqs. (12) and (13) related to the heat capacity were obtained from Bicerano.[31] The physical parameters of the studied resins are summarized in Table VI.

Processing conditions

The processing conditions used for the model simulations are summarized in Table VII.

RESULTS AND DISCUSSION

Effect of the take-up speed on the crystallinity profile

The effect of the take-up speed on the spinline crystallinity profile at 0.625 and 0.31 ghm for 5D49 hPP is shown in Figures 4 and 5, respectively. The model is shown to predict the experimental data well overall with the same set of material parameters (both rheological and SIC-related). An increase in the take-up speed results in an enhancement of the crystallization rate as indicated by the onset of crystallization closer to the die, which implies the effects of SIC. In the absence of any effect of orientational stress on the crystallization rate ($\xi = 0$, $n = 3$), crystallization is attributed solely to polymer undercooling (thermal crystallization); the crystallinity at the end of the spinline would be practically zero even at the lowest spinning speed (750 m/min), at which the available time for thermal crystallization would be highest (Fig. 4). This is due to the fact that the cooling rates in the spinline are enormously high (calculated to be of the order of 10^4–10^5°C/min) with respect to those of DSC quiescent crystallization experiments (10°C/min; Fig. 3). The fact that the crystallinity saturates at its ultimate value (~55%) at the end of the spinline, as illustrated by the data and captured by the model, is further proof that SIC is the controlling mechanism for spinline crystallization

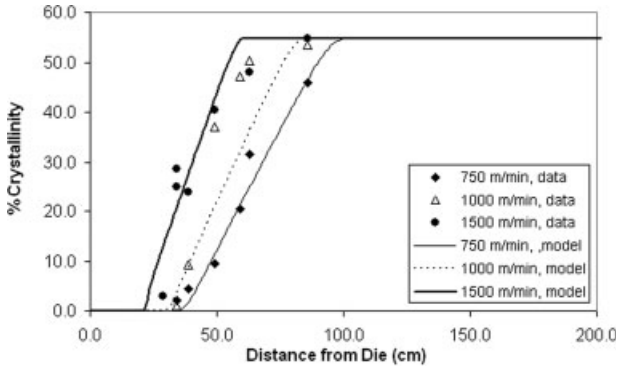

Figure 5 Measured and predicted crystallinity profiles along the spinline as a function of the take-up speed at 0.31 ghm for 5D49.

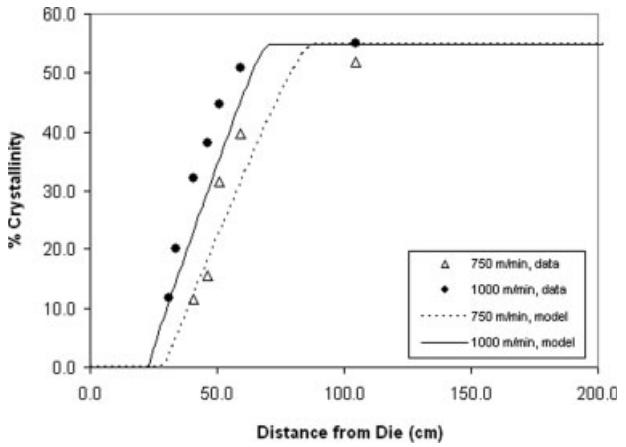

Figure 6 Measured and predicted crystallinity profiles along the spinline as a function of the take-up speed at 0.31 ghm for H502-25RG.

of hPP, driving the transformation to completion ($x \sim 100\%$).

Model comparisons with experimental data of the online crystallinity at different take-up speeds for H502-25RG hPP are shown in Figure 6. Similarly to 5D49 hPP, the model predictions are very good for H502-25RG with the same set of material parameters used for 5D49 simulations (the only difference is η_0, reflecting the difference in the molecular weights of the two materials). The effects of SIC are also evident for the H502-25RG resin (Fig. 6).

From Figures 4 and 5, it appears that model predictions are overall closer to experimental data at 0.31 ghm rather than at 0.625 ghm. It is speculated that this may be partially due to the lumped multifilament assumption in which each of the 60 filaments is considered to have equivalent heat-transfer characteristics [see eq. (2)]. At 0.625 ghm, filament cooling should not be as efficient as that at 0.31 ghm, so at 0.31 ghm filament cooling is expected to be more uniform across the filament bundle relative to the case of 0.625 ghm. Therefore, the lumped multifilament assumption should be more valid at 0.31 ghm than at 0.625 ghm, reflecting the better model predictions at 0.31 ghm. Nevertheless, model predictions at 0.625 ghm are still reasonable overall. We should also note that the material/molecular SIC parameters (ξ and F) were determined manually by a trial and error approach (see the Input Parameters section). A more rigorous parameter optimization procedure (e.g., particle swarm optimization[33]) may lead to improved model predictions, but this is beyond the scope of this article as the model predictions are considered good overall.

Along similar lines, we should also point out variations of the experimental data because the Raman crystallinity data are averages over the whole bundle of 60 filaments and not specific to a particular filament. Therefore, variations of the crystallinity profiles, such as those due to differences in filament cooling, cannot be captured with this experimental setup. This could reflect the observed overlap of the experimental crystallinity profiles at 750 and 1000 m/min at 0.625 ghm (Fig. 4), whereas one would expect that at 1000 m/min the crystallization rate would be faster than at 750 m/min. Similarly, in Figure 5 there seems to be an overlap of the experimental crystallinity profiles between 1000 and 1500 m/min, whereas one would expect the crystallization rate to be distinctly faster at 1500 m/min because of SIC effects.

Effect of the throughput on the crystallinity profile

The effect of the throughput on the spinline crystallinity profile at various spinning speeds for 5D49 hPP is shown in Figures 7–9. For all speeds and throughputs studied, the model predicts the experimental data very well, again using the same set of material parameters. For a given spinning speed, a reduction of the throughput results in an enhancement of the crystallization rate because of increased frozen spinline stress as a result of an enhanced cooling rate. This is further evidence for SIC controlling the spinline crystallization kinetics of hPP.

Effect of MFR on the crystallinity profile

The effect of MFR on the spinline crystallinity profile at 0.31 ghm and 750, 1000 m/min is shown in Figures 10 and 11, respectively. An increase in MFR results in slower crystallization kinetics (the onset of crystallization is at a position further away from the die). This is a result of SIC because under the same processing conditions, the higher MFR material (lower molecular weight and viscosity) will develop less spinline stress. We should note that the model captures quite well the difference in the crystalliza-

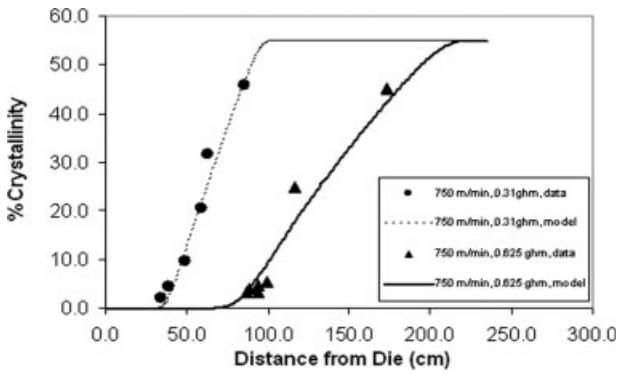

Figure 7 Measured and predicted crystallinity profiles along the spinline as a function of the throughput at 750 m/min for 5D49.

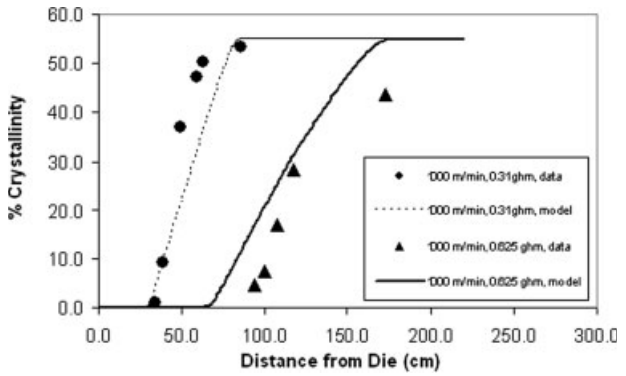

Figure 8 Measured and predicted crystallinity profiles along the spinline as a function of the throughput at 1000 m/min for 5D49.

tion rate of the 25 and 38 MFR materials with the same set of material parameters (except of course for η_0, which reflects the difference in MFR and thus the molecular weight).

Prediction of the spinline tension

Comparisons of model predictions with experimental data of the spinline tension (measured near the take-up roll) for both 5D49 and H502-25RG under a variety of processing conditions are shown in Figure 12. The model predictions compare quite favorably with the experimental data. Both the data and model indicate a more or less linear increase in the tension with the take-up speed in the range of 750–1500 m/min. The model nicely captures that the major factor in controlling the spinline tension is the take-up speed, whereas the throughput plays a secondary role. Finally, the model quantitatively captures the higher spinline tension of H502-25RG versus 5D49 hPP under the same processing conditions. This is due to the higher MFR of 5D49 and thus lower viscosity and spinline stress.

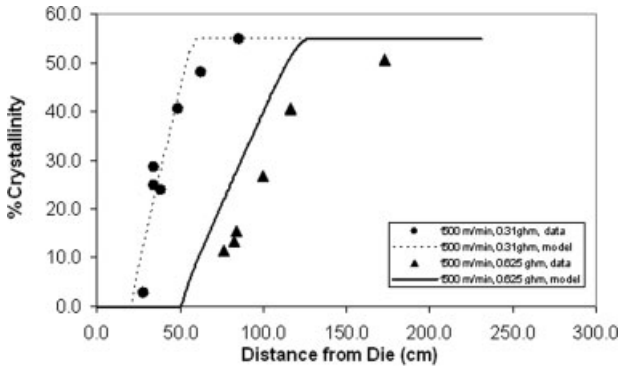

Figure 9 Measured and predicted crystallinity profiles along the spinline as a function of the throughput at 1500 m/min for 5D49.

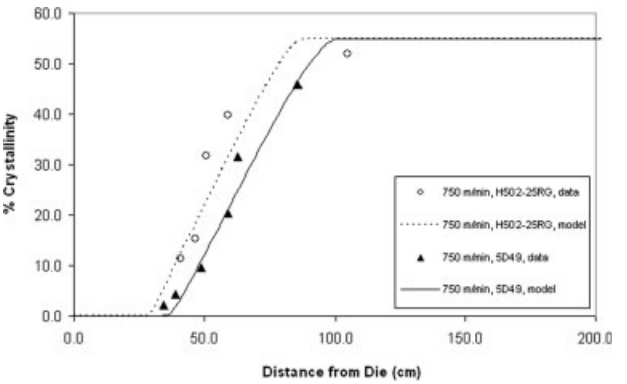

Figure 10 Effect of MFR on the spinline crystallization kinetics at 0.31 ghm and 750 m/min.

Prediction of freeze points/stick points

The model is capable of predicting the freeze point (i.e., the point in the spinline at which deformation ceases and the fiber velocity reaches a plateau value) as a function of resin characteristics (e.g., molecular weight, crystallization kinetics, and melt rheology) and fabrication conditions. An example is shown in Figure 13. For 5D49 hPP, the fiber velocity is predicted to increase along the spinline up to the freeze point (indicated by the arrows in Fig. 13), below which the velocity plateaus because of the ceasing of the extensional deformation. An increase in the take-up speed is predicted to result in a freeze point closer to the die (Fig. 13), reflecting the faster crystallization rate (Fig. 4).

In Figure 14, it is shown that there is a very good correlation of the model-predicted freeze point and the measured stick point (see the Experimental section) for 5D49 hPP for the whole range of process conditions investigated. This is reasonable because, from a physics point of view, the stick point is con-

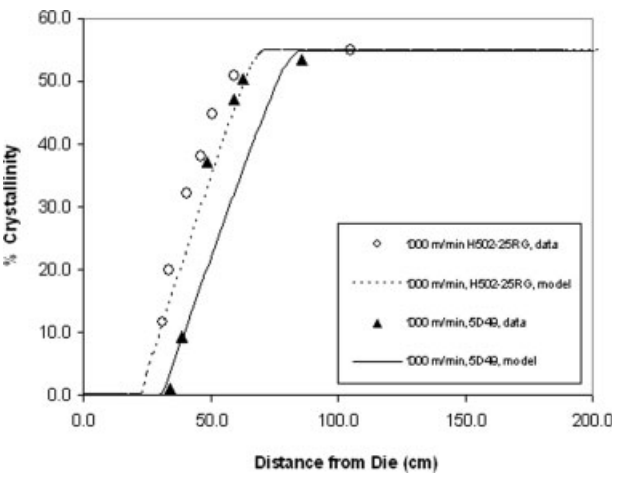

Figure 11 Effect of MFR on the spinline crystallization kinetics at 0.31 ghm and 1000 m/min.

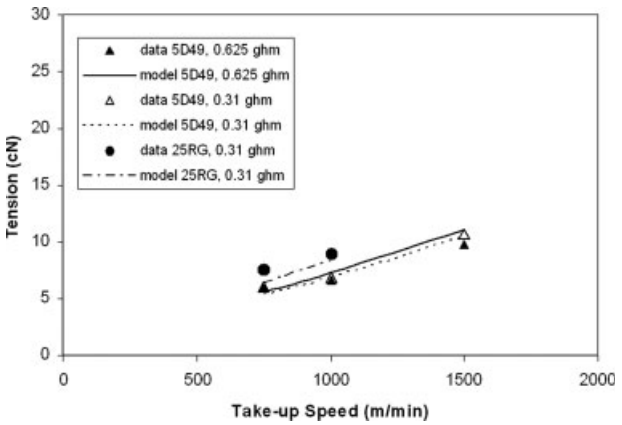

Figure 12 Measured and predicted spinline tension at the take-up wheels as a function of the take-up speed, throughput, and MFR.

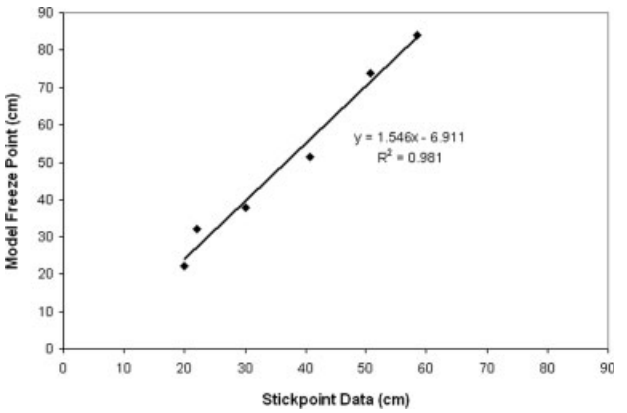

Figure 14 Correlation of the freeze point (model prediction) with the stick point (data) for 5D49 and the whole range of fabrication conditions studied in this work.

ceptually related to the freeze point. The freeze point originates from the occurrence of crystallization in the spinline resulting in locking-in of the molecular orientation and chain extension, thus reflecting the ending of the macroscopic deformation. On the other hand, the stick-point measurement gives an approximate point in the spinline at which the fiber bundle converts from a liquid-like state to a solid-like state. Since the stick-point measurement is not as rigorous as the online Raman crystallinity measurement, the stick point does not necessarily coincide with the model-predicted freeze point, as shown in Figure 14; however, a strong correlation exists between the two, and this is consistent with our conceptual consideration.

Because of the strong correlation of the stick point with the freeze point, we checked the predictive capability of the model for a normalized stick point. The freeze point and stick point were normalized by their respective values at a reference set of processing conditions, which were chosen to be 750 m/min and 0.625 ghm in this work. The comparisons are shown in Figure 15. The normalized stick point seems to coincide with the normalized freeze point to a good approximation, and this enhances our hypothesis on the correlation of the two variables. The good predictive capability of the model is worth noting because the same set of material parameters (F and ξ as well as the melt rheology parameters α, G, and N_o) were used for the predictions of Figures 14 and 15. Consistent with the stick-point data, the model quantitatively captures the relative shift of the freeze point toward the die with an increase of the take-up speed and decrease of the throughput. By analyzing Figures 14 and 15 with respect to Figures 4 and 5, we conclude that the freeze point and stick point are associated with the onset of spinline crystallization. Most of the crystallization occurs below the freeze point/stick point. Raman crystallinity and stick-point data as well as model predictions suggest that a very small amount of crystallinity is able to

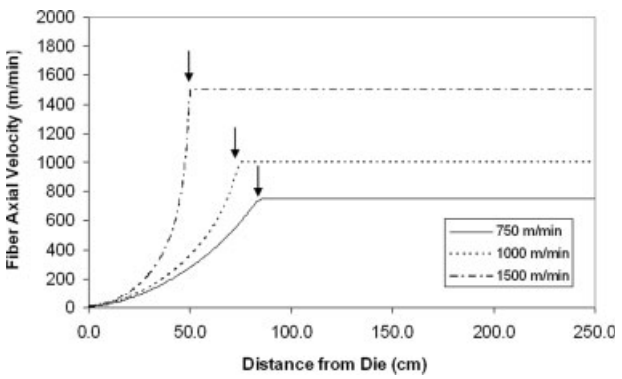

Figure 13 Predicted fiber velocity profiles along the spinline for 5D49 at 0.625 ghm and various spinning speeds. The arrows indicate the position of the model-predicted freeze points.

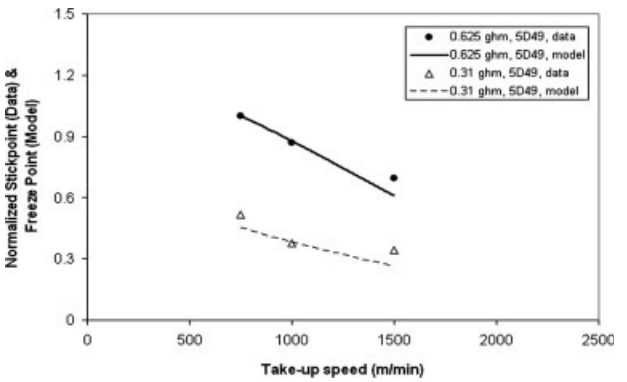

Figure 15 Comparison of the normalized freeze point (model) with the normalized stick point (data) as a function of the take-up speed at various throughputs for 5D49. All stick-point data and freeze-point model predictions were normalized by their respective values at 750 m/min and 0.625 ghm for consistency.

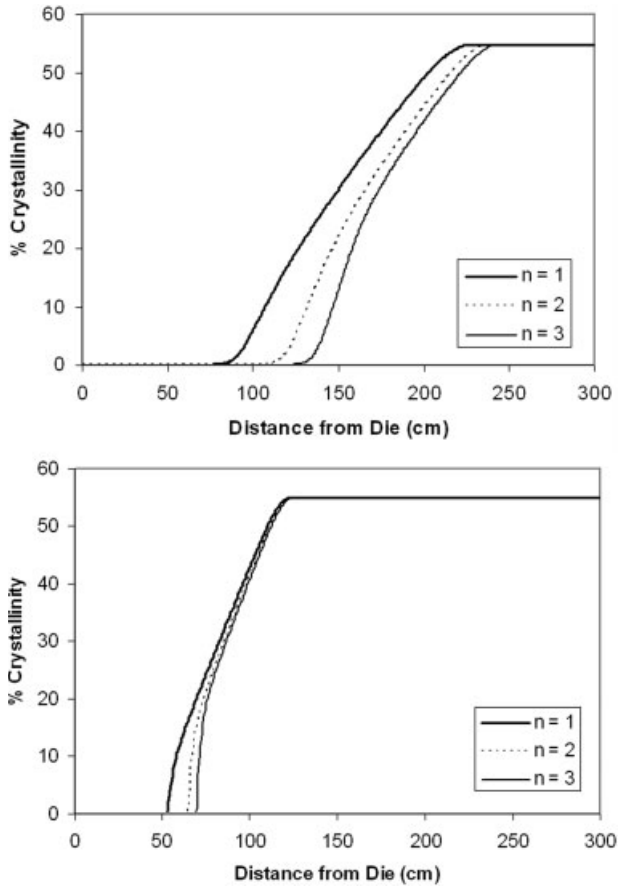

Figure 16 Effect of Avrami exponent n on the predicted spinline crystallinity profiles under SIC conditions at 0.625 ghm: 750 (top) and 1500 m/min (bottom). The SIC material parameters of Table V were used in the simulations. All other processing conditions are listed in Table VII.

lock in the structure and stop the extensional deformation. This finding is consistent with SIC behavior in fiber spinning documented by Doufas et al.[5,6] and Spruiell and coworkers[3,4,34] Finally, these results and trends also render the stick point a useful quantity for assessing spinline behavior and crystallization kinetics on a purely comparative basis for different resins and processing conditions.

Effect of Avrami exponent *n*

The effect of n [eq. (6)] on the crystallization kinetics under extreme flow deformation conditions studied in this work is depicted in Figure 16. The SIC material parameters used in the simulations are shown in Table V. With an increase of n from 1 (uniaxial crystal growth) to 3 (spherulitic crystal growth), the onset of crystallization (and thus the freeze point) is shifted away from the die, and the crystallization kinetics accordingly become slower for both take-up speeds studied, as physically expected. The effect of exponent n is greater at 750 m/min than at 1500 m/min. This is considered to be physically reasonable because n is mostly related to thermal crystallization effects. Therefore, at the lowest take-up speed (750 m/min) at which SIC is of less significance with respect to the highest speed (1500 m/min), the impact of thermal crystallization, reflected in exponent n, on the overall crystallization rate is more pronounced.

The shape of the spinline crystallinity profiles does not change with the variation of n overall (Fig. 16). The onset of crystallization is merely shifted at a position away from the die with an increase of n. Therefore, in principle, for a given value of n, one could calibrate the SIC parameters ξ and F, which yield equally good fits and predictions of crystallinity profiles, with those shown in Figures 4–11. However, under SIC conditions and because of the uniaxial molecular orientation involved during the drawing process, we postulate that it makes more physical sense to take n as 1 in the SIC simulations, which is consistent with the original D–M model.[5] Therefore, n is not an adjustable parameter in the D–M model; rather, it is set to 1 in agreement with its inherent approximations.

Discussion of the physics and robustness of the original D–M two-phase model[5–7]

The original D–M[5–7] SIC model employed in this work was found to be numerically robust in the simulation of PP melt spinning over a wide range of industrial processing conditions and presents very good overall predictive capability of experimental data. Below are some comments regarding the physics and robustness of the D–M model[5–7] as well as comparisons with a modified algorithm proposed by Shrikhande et al.:[35]

- Given the very good predictive capability of the original D–M SIC model[5–7] in terms of spinline crystallinity profiles, fiber tension, and freeze points (correlated to measured stick points), the introduction of both amorphous and semicrystalline phases at the start of the integration algorithm[35] was not found to be advantageous or necessary in this work.
- We consider that the introduction of the semicrystalline phase at T_m^0 of the polymer in the spinline,[5–7] although an approximation, has more physical significance than the introduction of both phases at the start of the computational domain ($z = 0$),[35] at which the system is completely molten and no crystallization takes place.
- In our view, any apparent model discontinuity [e.g., in the slope of a semicrystalline orientation variable (S_{zz}) at the onset of crystallization; see Fig. 7 of ref. 35] due to the introduction of the

semicrystalline phase at the melting temperature is physically and conceptually consistent with the discontinuity associated with the crystallization phenomenon as a first-order phase transition. In other words, crystallization is by definition a discontinuous physical process, and so model discontinuity at the onset of crystallization in the spinline is physically justified and expected. On the other hand, this apparent model discontinuity dissipates quite fast (as shown in Fig. 7 of ref. 35) and does not affect the numerical robustness or prediction of macroscopic variables, at least for the steady-state simulations.

- The flow enhancement factor coupling the trace invariant of the total extra stress tensor to the crystallization kinetics (related to the material parameter ξ)[5–7] in the original model is found to be applicable to the simulation of PP fiber spinning, leading to good overall predictive capability of spinline crystallinity profiles for a wide range of processing conditions, as shown in Figures 4–11. The coupling of SIC kinetics to the trace of the extra stress tensor is conceptually consistent with nucleation theory, as the trace stress invariant is proportional to the Helmholtz stored free energy[36] for flexible bead–spring constitutive models. Since the solid phase in the D–M model[5–7] is actually semicrystalline, both melt chain segments and amorphous regions in the semicrystalline phase could theoretically affect SIC kinetics. This is reflected in the inclusion of both amorphous and semicrystalline stresses in the crystallization kinetics. We postulate that this feature could potentially enable the inclusion of secondary crystallization effects in the model (where secondary crystallization is considered to be affected partially by the orientation and locked-in stresses of amorphous chain segments in the semicrystalline solid).
- The premise of the original D–M model[5–7] is that the system is driven to complete phase transformation ($x \rightarrow 1$) at the end of the spinline under high-speed spinning conditions (no remaining melt phase in the fiber, so ~100% is semicrystalline solid). This is achieved with the flow enhancement factor coupling both melt and semicrystalline phase stresses to the crystallization kinetics. Under low-speed spinning conditions, the model does predict $x < 1$[6] because SIC is not significant and thermal crystallization dominates. Under high-speed spinning conditions, the system is naturally driven to $x \rightarrow 1$ in the original model (dx/dz^* naturally goes through a maximum before dropping;[35] this similar to low-speed spinning conditions[6]), and termination of the crystallization calculations at $x = 0.997$ is reasonable (practically zero statistical links remain in the melt chains), without any of the predictions or model self-consistency being affected. This concept is reasonably applicable to PP fiber spinning because the crystallinity at the end of the spinline does not appear to significantly depend on the take-up speed, at least for the processing conditions studied in this work (e.g., see Figs. 5 and 6). We propose that any dependence of final crystallinity on the spinning conditions[35] could be alternatively captured via the development of a theory/relationship of ultimate crystallinity ϕ_∞ on the orientation and/or stress. Nevertheless, as pointed out by Doufas and coworkers,[5,8] there is no unique way of performing the coupling in SIC kinetics, and so the coupling could be system-specific and should be chosen to maximize the model predictive capability.
- We should point out that the D–M model[5–7] is self-consistent, in the sense that the melt conformation tensor gradient (dc^*_{rr}/dz^*) undergoes a secondary downward peak (Fig. 7 of ref. 35) during the evolution of crystallization that is physically justified by shortening of the melt amorphous chains up to completion of the transformation under high-speed conditions and satisfaction of incompressibility. Therefore, the secondary peak of dc^*_{rr}/dz^* reflects the physics of the process and is not a numerical anomaly. The modified algorithm of Shrikhande et al.[35] does not predict a secondary spike of dc^*_{rr}/dz^* simply because the transformation is not driven to completion under high-speed conditions (Figs. 7 and 8 of ref. 35). As $x \rightarrow 1$, the extra stress of the melt vanishes in the original model as it should (no remaining melt statistical segments; see Fig. 9 of ref. 35), the system stress is locked in, and the stiff semicrystalline phase carries all of the stress as expected.[5]
- To initialize the simulation, the seamless boundary condition formalism of the modified algorithm[35] postulates arbitrary values for the second derivative of the axial velocity [eq. (17) of ref. 35], whose effect on model predictions and numerical stability is not known in the general case (e.g., polyolefin-based systems). On the other hand, the formalism of the original D–M model[5–7] warranties continuity in the axial velocity and velocity derivatives during the transition from the single-phase (melt) model to the two-phase model at the melting temperature, without the need of assuming a value for any of the velocity derivatives.
- The constitutive equation of the melt phase of the D–M model[5–7] is a modified Giesekus equation including the finite extensibility of the poly-

mer chains captured by nonlinear force factor E. Neglecting E (i.e., original Giesekus model), as is the case in the modified algorithm,[35] is not recommended in the general case because the original Giesekus model is not capable of capturing the melt extensional rheology of polyolefin melts, which is expressed in terms of rheotens tensile force curves as demonstrated by Doufas.[13] For example, the original Giesekus model[35] cannot capture the plateau in the tensile force (melt strength); instead, it demonstrates a monotonically increasing force with the take-up speed,[13] whereas the modified Giesekus model does capture the plateau in the tensile force[13] and has greater flexibility in fitting and predicting rheotens data. The relatively small number of statistical segments per network strand (e.g., $N_o = 25$) for polyolefins[13] further justifies the use of the molecular factor E. Therefore, it is concluded that the modified Giesekus constitutive model is more appropriate for fiber-spinning simulations of polyolefin systems.

- The predictions of the original D–M SIC model[5–7] versus the modified algorithm[35] are practically identical in terms of measurable macroscopic quantities (e.g., fiber velocity and total extra stress, the latter related to fiber tension, which is measurable), as shown in Figures 7 and 9 of ref. 35. In our view, it is difficult to claim an advantage for prediction of other model variables such as conformation/orientational tensors (e.g., c^*_{rr} and S_{zz}; see Fig. 7 of ref. 35) or amorphous phase stress (e.g., Fig. 9 of ref. 35) because these variables are not really measurable quantities.

CONCLUSIONS

The original D–M[5–7] two-phase microstructural/constitutive model for SIC has been expanded to polyolefin systems and validated for its predictive capability of online Raman crystallinity and spinline tension data for two Dow hPP resins, H502-25RG and 5D49, with MFRs of 25 and 38, respectively. The material parameters—inputs to the model—have been shown to be obtained from laboratory-scale material characterization data, namely, oscillatory dynamic shear, rheotens (melt extensional rheology), and DSC data. The same set of two SIC material/molecular parameters (ξ and F) has been shown to be capable of predicting the crystallinity profiles along the spinline and fiber tension very well overall for a variety of industrial fabrication conditions. The model predicts the freeze point, which has been shown, for the first time, to correlate very well with the measured stick point (i.e., the point in the spinline at which the fiber bundle converts from a solid-like state to a liquid-like states and sticks to a solid object such as a glass rod). The model quantitatively captures the effects of the take-up speed, throughput, and MFR on the crystallization rate due to SIC effects. This validated modeling approach has been used to guide fiber spinning for rapid product development.

The original D–M two-phase model[5–7] employed in this work has been found to be numerically robust for the simulation of steady PP fiber spinning over a wide range of processing conditions without issues of discontinuities due to the onset of the two-phase constitutive formulation downstream of the die face, at which crystallization more realistically begins. Given the good predictive capability of the original D–M model,[5–7] the introduction of both phases at the start of the integration algorithm[35] has not been found to be advantageous or necessary in this work. The flow enhancement factor coupling the total extra tensor trace invariant to the crystallization kinetics (related to the material parameter ξ)[5–7] has been found to be applicable to the simulation of PP melt spinning, leading to good overall predictive capability of spinline crystallinity profiles. Finally, because of the capturing of the physics of PP fiber spinning and the very good model predictive power, the approximations of the original D–M model[5–7] are asserted to be reasonable.

Part of this work was presented at the 2007 Society of Plastics Engineers Conference in Cincinnati, OH (Annu Tech Conf Tech Pap Proc 2007, 1464). The authors thank Marc Mangnus for generating the rheological data that were used to extract the material parameters needed for the model simulations and David Gillespie and Mike Nelson for providing the molecular weight data. Special thanks are due to Ed Knickerbocker and Zeke Rios for their help with fiber spinning.

References

1. Paradkar, R. P.; Knickerbocker, E.; Patel, R. M.; Doufas, A. K. Soc Past Eng Tech Pap Annu Tech Conf 2007, 1459.
2. Paradkar, R. P.; Knickerbocker, E.; Patel, R. M.; Doufas, A. K. J Appl Polym Sci, to appear.
3. Lu, F.; Spruiell, J. E. J Appl Polym Sci 1987, 34, 1541.
4. Bond, E. B.; Spruiell, J. E. J Appl Polym Sci 2001, 82, 3223.
5. Doufas, A. K.; McHugh, A. J.; Miller, C. J Non-Newtonian Fluid Mech 2000, 92, 27.
6. Doufas, A. K.; McHugh; A. J.; Miller, C.; Immaneni, A. J Non-Newtonian Fluid Mech 2000, 92, 81.
7. Doufas, A. K.; McHugh, A. J. J Rheol 2001, 45, 403.
8. Doufas, A. K.; Dairanieh, I. S.; McHugh, A. J. J Rheol 1999, 43, 85.
9. Bird, R. B.; Curtiss, C. F.; Armstrong, R. C.; Hassager, O. Dynamics of Polymeric Liquids, 2nd ed.; Wiley: New York, 1987; Vol. 2.
10. (a) Doufas, A. K.; Butler, T. Soc Past Eng Tech Pap 2003, vol LXI, 3261; (b) Doufas, A. K.; McHugh, A. J. J Rheol 2001, 45, 1085.
11. Zheng, R.; Kennedy, P. K. Proc World Congress Chem Eng 2001, 6.
12. Zheng, R.; Kennedy, P. K. J Rheol 2004, 48, 823.

13. Doufas, A. K. J Rheol 2006, 50, 749.
14. Brandrup, J.; Immergut, E. H.; Grulke, E. A. Polymer Handbook, 4th ed.; Wiley-Interscience: New York, 1999.
15. Bershstein, V. A.; Egorov, V. M. Differential Scanning Calorimetry of Polymers: Physics, Chemistry, Analysis, Technology; Ellis Horwood Ltd.: London, UK; 1994.
16. Cohen, A. Rheol Acta 1991, 30, 270.
17. Denn, M. M. In Computational Analysis of Polymer Processing; Pearson, J. R. A.; Richardson, S. M., Eds.; Applied Science: London, 1983.
18. Matsui, M. Trans Soc Rheol 1976, 20, 465.
19. Denn, M. M. Ind Eng Chem Res 1996, 35, 2842.
20. Dutta, A. Text Res J 1987, 57, 13.
21. Yasuda, H.; Ishihara, H.; Yanagawa, H. Sen-I-Gakkaishi 1978, 34, 20.
22. Ishihara, H.; Hayashi, S.; Ikeuchi, H. Int Polym Process 1989, 4, 91.
23. Harvey, A. D. Doufas, A. K. AIChE J 2007, 53, 78.
24. Bird, R. B.; Armstrong, R. C.; Hassager, O. Dynamics of Polymeric Liquids, 2nd ed.; Wiley: New York, 1987; Vol. 1.
25. Ghijsels, A.; Chippeleir, J. D. Int Polym Process 1994, 9, 252.
26. Laun, H. M.; Schuch, H. J Rheol 1989, 33, 119.
27. Munstedt, H.; Laun, H. M. Rheol Acta 1981, 20, 211.
28. Muke, S.; Ivanov, I.; Kao, N.; Bhattacharya, S. N. J Non-Newtonian Fluid Mech 2001, 101, 77.
29. Patel, R.; Spriuell, J. Polym Eng Sci 1991, 31, 730.
30. Nakamura, K.; Katayama, K.; Amano, T. J Appl Polym Sci 1973, 17, 1031.
31. Bicerano, J. Prediction of Polymer Properties, 3rd ed.; Marcel Dekker: New York, 2002.
32. Ziabicki, A. Fundamentals of Fibre Formation; Wiley: New York, 1976; p 75.
33. Kennedy, J.; Eberhart, R. C. Swarm Intelligence; Morgan Kaufmann: San Mateo, CA, 2001.
34. Spruiell, J. E.; Lu, F.-M.; Richeson, G. J Appl Polym Sci 1996, 62, 1965.
35. Shrikhande, P.; Kohler, W. H.; McHugh, A. J. J Appl Polym Sci 2006, 100, 3240.
36. Marrucci, G. Trans Soc Rheol 1972, 16, 321.